Supplemental Online Materials

The Michigan Infrared Combiner (MIRC) is a new instrument on the Georgia State University CHARA interferometric array; MIRC and the CHARA Array have both been described in detail (*S1, S2*) and MIRC commissioning results have already been presented (*S3*). Here in the supplemental online materials, we present validation studies of our data pipeline and image reconstruction methods.

MIRC is an image plane combiner which currently combines light from four CHARA telescopes simultaneously. The four CHARA beams are filtered by single-mode fibers and the beams are rearranged into a 1-dimensional non-redundant pattern and brought to a focus. These overlapping beams create six interference fringes, each with a unique spatial frequency. The pattern is then focused by a cylindrical lens into a "line" of fringes which are subsequently dispersed by a simple spectrograph with spectral resolution $\Delta\lambda \sim 0.035\mu$m. Fast readout of the Rockwell PICNIC camera (frame time 5.5 ms) effectively freezes the atmosphere under most seeing conditions in the infrared. In this way, MIRC can measure 6 visibilities, 4 closure phases, and 4 triple amplitudes simultaneously over 8 spectral channels spanning the astronomical H-band ($\lambda = 1.50 - 1.74\mu$m).

Here we briefly outline the MIRC data analysis method. After background subtraction, the fringe patterns are analyzed by taking the Fourier transform. From this intermediate data, the fringe phases and amplitudes can be combined to form the triple product, often expressed as complex number that can be coherently averaged (the angle argument is the closure phase) (*S4*). The power spectra are also accumulated for visibility-squared estimation. Bias in the power spectrum is subtracted using a combination of "foreground" observations (data taken with halted delay lines) and measurements using high spatial frequencies immune to contamination by true fringe power.

The above procedures result in tabulations of uncalibrated squared-visibilities and (complex) triple amplitudes. In order to calibrate the amplitudes of these quantities, we must estimate how much light is injected into the fibers during fringe measurements. We use spinning choppers to partially obscure each input pupil during fringe acquisition, chopping each beam at a unique frequency (25 Hz, 30 Hz, 35 Hz, 40 Hz). Since fringes are spatially-modulated, we can use the temporally-chopped intensities to obtain an estimate of the fiber coupling efficiencies simultaneous with fringe measurements.

At this stage in the analysis, individual data files have been calibrated but no estimates of the system visibilities have been made. Since we have a single-mode fiber system, the system visibilities are highly stable, however the image-plane combiner is susceptible to temporal decoherence since the 5.5 ms exposure time is not short enough to completely freeze turbulence. We track these and any other changes in system visibility by observing calibrator objects with known sizes, in this case γ Lyr and υ Peg with estimated uniform disk diameters of 0.74 ± 0.10 mas (*S5*) and 1.05 ± 0.05 mas (MIRC/CHARA) respectively. While uncertainties in calibrator diameters are often the dominant error for long baseline interferometers like the CHARA Array, such errors are generally not important for Altair which is unusually highly-resolved – our dominant errors are from imprecise calibration of mean fiber coupling and fast changes in atmospheric coherence time.

In order to validate our pipeline and imaging procedures, we carried out observations of the binary ι Peg. This binary is well-suited for calibration, having been observed by IOTA, NPOI, PTI, and MIRC/CHARA. Using ι Peg we have calibrated our "closure phase sign" which removes the $180°$ ambiguity in imaging. Furthermore, we have confirmed our wavelength calibration at the 0.3% level through comparison with previously published and new PTI measurements (*S6*). The top panels of Figure S1 show the snapshot Fourier coverage of our ι Peg observations from UT2006Sep02 as well as our calibrated visibility-squared data compared to

the binary model fit.

ι Peg represented a suitable target for validation of the MACIM imaging algorithm (*S7*) as well. The bottom panels of Figure S1 show the MACIM image reconstruction of the ι Peg binary along with the best-fit binary model; these results are consistent with the prediction from the orbit (*S6*). The MACIM image is in excellent agreement with the model, including the size determinations of the two stars. We also show the imaging results using the CLEAN algorithm (*S8*) with self-calibration. A detailed analysis of ι Peg will follow in a subsequent paper.

Since imaging with optical interferometry is still novel, we present here the calculated interferometric observables from our MACIM/MEM image presented in Figure 2 of the mainn report. Figures S2-4 contain all the individual data points used in this Report and they are compared with the imaging results. As found in other studies (*S3, S9*), the closure phase quantities are particularly robust and precise, showing none of the calibration difficulties typically encountered for measurements of visibility amplitudes. The calibrated data for Altair, stored in the Optical Interferometry data exchange format (OI-FITS) (*S10*), are available from the authors.

The final topic to discuss is the special imaging procedure for Altair. Firstly, we emphasize that use of MEM for interferometric imaging is standard practice (*S11, S12*) and the specific program MACIM (*S7*) has been validated on other test data (*S13*). Hence, we will not explain the fundamentals of interferometric imaging here or why specialized software is required for optical interferometers (*S10*), but rather refer the reader to the extensive literature (*S9, S14–S17*).

For imaging, we treated each wavelength channel as providing a distinct set of (u,v) plane coverage, ignoring any wavelength-dependence of the image itself – this procedure is sometimes referred to as wavelength-super-synthesis. This assumption is well-justified for infrared intensities of hot stars since the relative intensities across the photosphere for the Altair model

are nearly identical at 1.5μm, 1.65μm, and 1.8μm, showing relative distortions of $<0.5\%$. This level of inaccuraciy is much less than our observed temperature reconstruction errors of 4%. Note that our von Zeipel modeling code did treat this wavelength-dependence better by splitting the H band into 4-different sub-bands for fitting to the wavelength-dependent visibility and closure phases data.

The main difficulty in imaging the surface of a star is that the photospheric emission is expected to show a sharp fall-off at the limb. In terms of Fourier modes, this sharp cutoff is encoded in very long baseline visibilities which can not be observed. This in combination with the MEM procedure causes extensive "spreading out" in a reconstructed image, with more spreading happening where we lack the longest baseline data. From this perspective, we identify contradictory goals for the imaging procedure – smooth out the image as much as possible except right at the edge where we expect the sharp cutoff in emission. This problem is similar to that encountered by others (*S18*) attempting to image diffuse circumstellar material surrounding an unresolved point source. In the latter case, the imaging procedure was stabilized by using a point-source model as an "image prior" to the MEM procedure, based on a priori knowledge of the target under scrutiny.

For the imaging reported here, we used a uniform ellipse as a prior to the MACIM/MEM imaging. For the given elliptical prior, we ran the MACIM/MEM algorithm and found the image with maximum entropy fitting the data with a $\chi_\nu^2 \sim 1$. This procedure was robust – the MEM prior naturally limited the flux inside the elliptical boundary while the Maximum Entropy maximization tended to spread out the flux as much as possible consistent with the data itself.

The main complication in applying the above procedure is that we do not know *a priori* which ellipse to choose for our MEM prior. One could use the uniform ellipse derived from short baseline data, e.g., from the PTI data of Van Belle et al. (*S19*); however, one realizes that this is not optimum since the best-fit uniform ellipse underestimates the actually photospheric

4

boundary of an oblate star with gravity darkening (in the case of Altair by ~5%). In order to keep our imaging procedure general and avoid a bias through our choice of one specific elliptical prior, we carried out MACIM/MEM imaging on a grid of 500 different uniform ellipses spanning a range of possible sizes, elongations, and position angles. As expected, the "entropy" of the final image varied depending on the prior we adopted and it was a simple matter to find the global Maximum Entropy image from the ensemble.

As a final check on our calibration consistency, we carried out the above imaging procedures on the MIRC/CHARA data split by observing night. Figure S5 shows the final MACIM/MEM images for the two nights separately. Based on the variation between the two independent images, we estimate the photometric uncertainty in the final reconstruction to correspond to $\pm 4\%$ in intensity across the photosphere (with a worst case $\pm 10\%$ – near the limb of the star). The high degree of similarity gives us confidence that the final image reconstruction is not corrupted by night-to-night calibration errors.

Lastly, we comment on some confusion in the literature. Unfortunately the first published results on Altair (*S19*) inadvertently had the (u,v) coordinates switched. This mistake was compounded in the next paper on Altair, Ohishi et al. (*S20*) from NPOI, which also made a coordinate mistake. These errors were noticed by Domiciano de Souza (*S21*) who attempted a correction in order to combine all the data together in a self-consistent way (although this was not mentioned in the paper itself). Most recently, Peterson et al. (*S22*) re-analyzed the original NPOI data, correcting the UV coordinate mistakes and pointing out the original PTI errors. However, this paper appears to have gotten the closure phase calibration incorrect – causing a $180°$ rotation in their published synthetic model images. In most cases, these errors affected only the inferred viewing orientation of Altair, thus they did not impact the astrophysical interpretation of the Altair data.
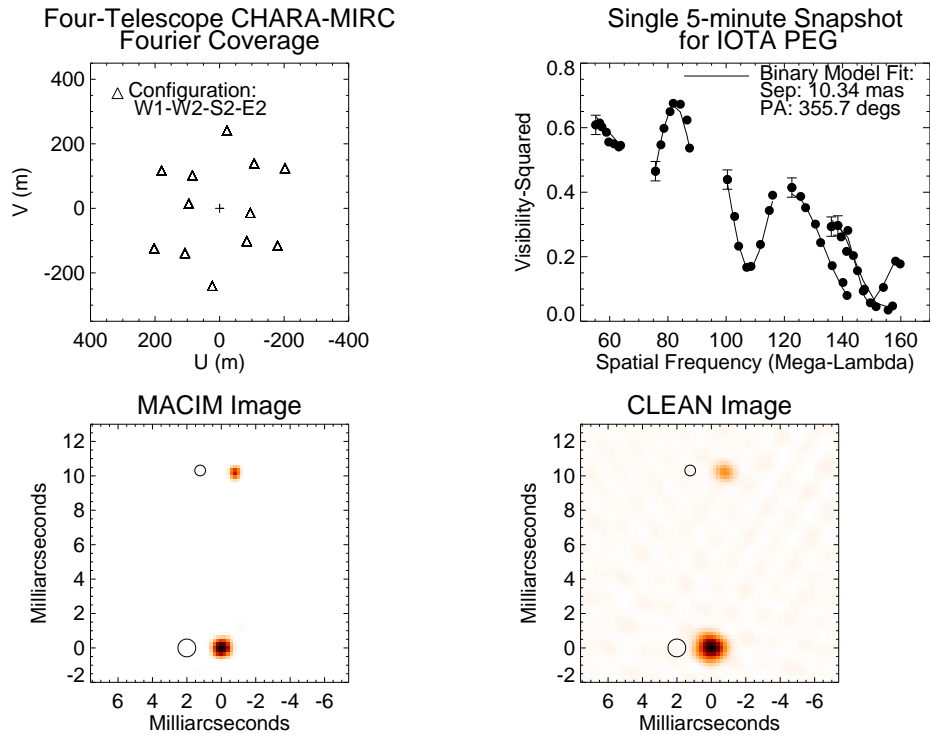
Figure S1: These four panels validate the MIRC/CHARA pipeline and the MACIM image reconstruction software. The top left panel shows the snapshot 4-telescope Fourier coverage for an observation of the calibration binary ι Peg on UT 2006 Sep 02. The top right panel shows the calibrated squared-visibility data along with the best-fit binary model (representative errors are shown only for long-wavelength channel for clarity). The bottom panels show a comparison of the image reconstructions using the MACIM and CLEAN algorithms with the best-fit binary model (circles offset 2 mas to the east).
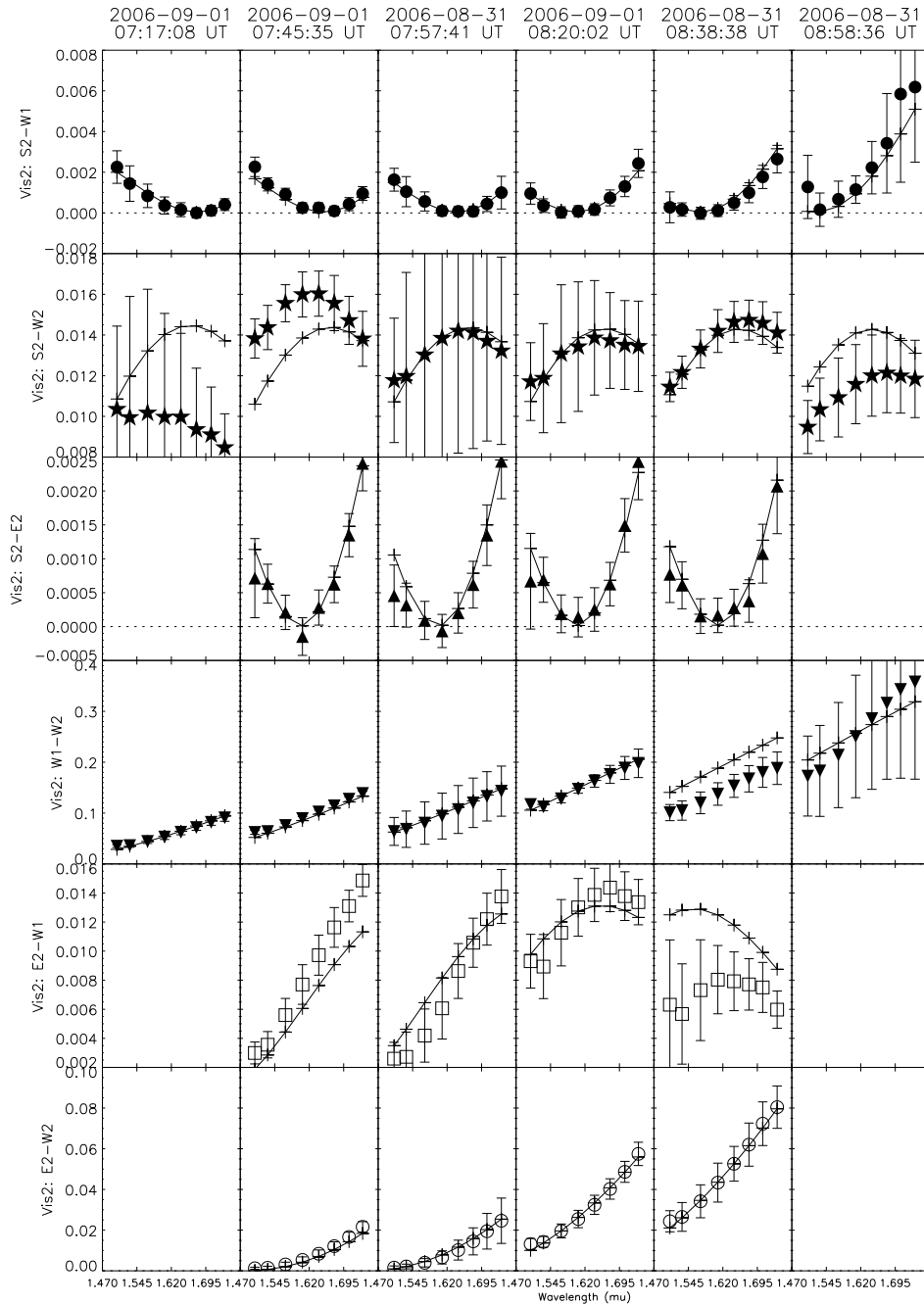
Figure S2: This figure shows the squared-visibilities (with errors) observed for Altair along with the calculated values from the MACIM/MEM image (line with crosses) presented in left panel of Figure 2. Each column is a different observing time while each row represents a different baseline. Inside each panel, the x-axis shows the wavelength of the spectrometer channels. Note that the visibility nulls shown above for baselines S2-W1 and S2-E2 are *second nulls* while the visibilities in E2-W2 and E2-W1 baselines are slightly before the first null.
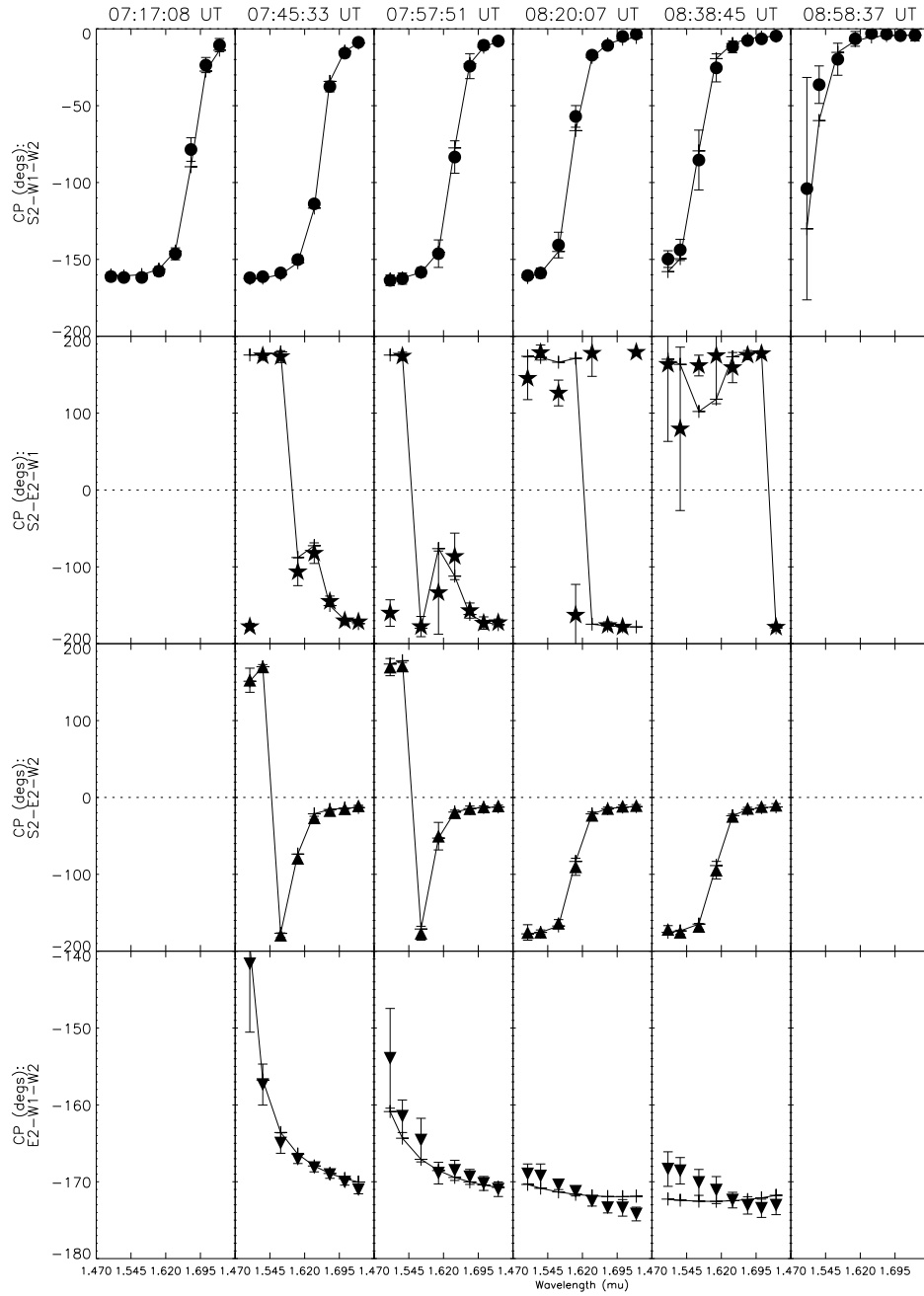
Figure S3: All closure phase measurements are shown for the Altair observations along with results from MACIM/MEM image (line with crosses). Note that the closure phase has a 360° phase ambiguity, thus a phase of +180° and -180° are identical in the panels above. The columns are different times and the rows represent different closure triangles.
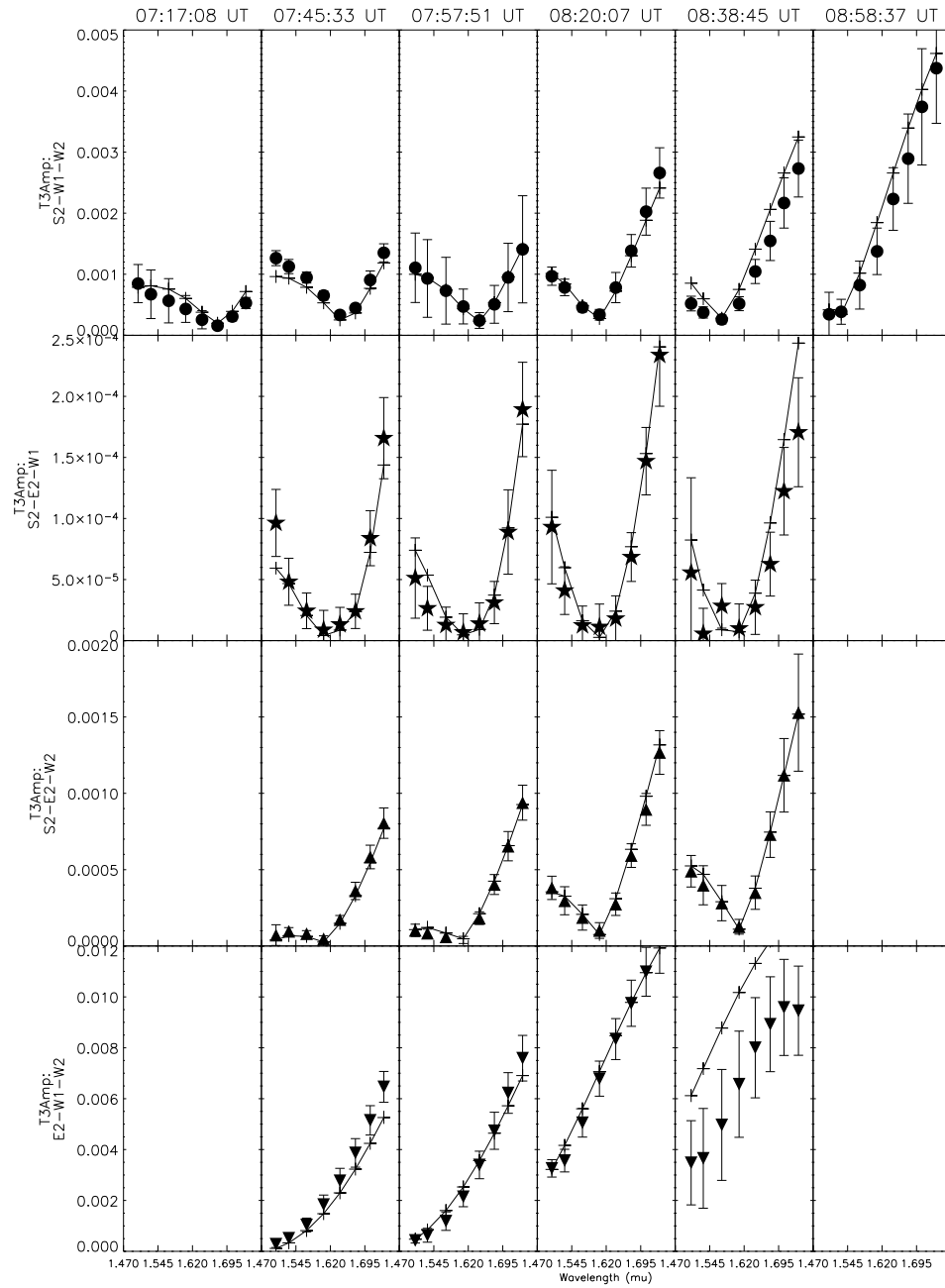
8

Figure S4: All triple amplitude measurements are shown for the Altair observations along with results from MACIM/MEM image (line with crosses). The columns are different times and the rows represent different closure triangles.
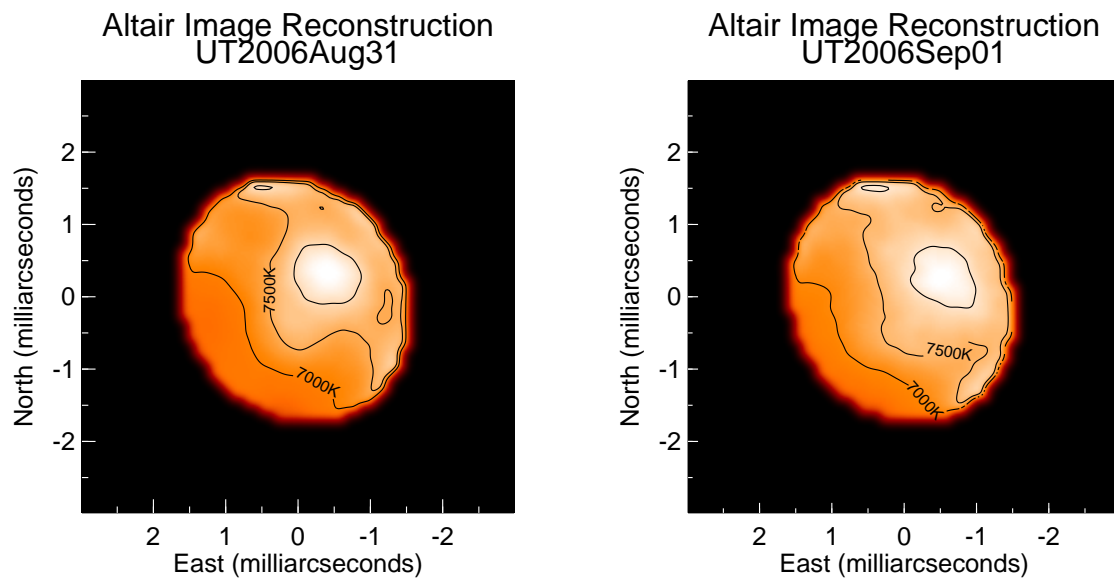
Figure S5: Similar to Figure 2 of main Report, except here we compare imaging results from two independent data sets. These image reconstructions agree at the 4% level rms, with maximum deviations of 10% near the limb.

References and Notes

S1. T. A. ten Brummelaar, *et al.*, ApJ **628**, 453 (2005).

S2. J. D. Monnier, J.-P. Berger, R. Millan-Gabet, T. A. Ten Brummelaar, *SPIE v.5491. (ed. Traub)*, W. A. Traub, ed. (2004), pp. 1370–+.

S3. J. D. Monnier, *et al.*, *SPIE v.6268 (eds. Monnier, Schöller Danchi)* (2006).

S4. J. D. Monnier, *Reports of Progress in Physics* **66**, 789 (2003).

S5. S. K. Leggett, *et al.*, A&A **159**, 217 (1986).

S6. A. F. Boden, *et al.*, ApJ **515**, 356 (1999).

S7. M. J. Ireland, J. D. Monnier, N. Thureau, *SPIE v.6268 (eds. Monnier, Schöller, Danchi)* (2006).

S8. J. A. Högbom, A&AS **15**, 417 (1974).

S9. J. D. Monnier, *et al.*, ApJ **602**, L57 (2004).

S10. T. A. Pauls, J. S. Young, W. D. Cotton, J. D. Monnier, PASP **117**, 1255 (2005).

S11. R. Narayan, R. Nityananda, ARA&A **24**, 127 (1986).

S12. P. G. Tuthill, J. D. Monnier, W. C. Danchi, E. H. Wishnow, C. A. Haniff, PASP **112**, 555 (2000).

S13. P. R. Lawson, *et al.*, *SPIE v.6268 (eds. Monnier, Schöller, Danchi)* (2006).

S14. T. J. Cornwell, P. N. Wilkinson, MNRAS **196**, 1067 (1981).

S15. T. J. Pearson, A. C. S. Readhead, ARA&A **22**, 97 (1984).

S16. J. E. Baldwin, *et al.*, A&A **306**, L13+ (1996).

S17. C. A. Hummel, *et al.*, AJ **125**, 2630 (2003).

S18. J. D. Monnier, *et al.*, ApJ **605**, 436 (2004).

S19. G. T. van Belle, D. R. Ciardi, R. R. Thompson, R. L. Akeson, E. A. Lada, ApJ **559**, 1155 (2001).

S20. N. Ohishi, T. E. Nordgren, D. J. Hutter, ApJ **612**, 463 (2004).

S21. A. Domiciano de Souza, *et al.*, A&A **442**, 567 (2005).

S22. D. M. Peterson, *et al.*, ApJ **636**, 1087 (2006).